Energy & Environmental Science

Non-Fullerene Acceptors with Direct and Indirect Hexa-fluorination Afford >17% Efficiency in Polymer Solar Cells

Journal:	*Energy & Environmental Science*
Manuscript ID	EE-ART-10-2021-003225.R1
Article Type:	Paper
Date Submitted by the Author:	02-Dec-2021
Complete List of Authors:	Li, Guoping; Northwestern University, Chemistry; Northwestern University, Department of Chemistry, the Center for Light Energy Activated Redox Processes (LEAP), and the Materials Research Center (MRC) Feng, Liang-Wen; Northwestern University, Department of Chemistry, the Center for Light Energy Activated Redox Processes (LEAP), and the Materials Research Center (MRC) Mukherjee, Subhrangsu; National Institute of Standards and Technology Material Measurement Laboratory Jones, Leighton; Northwestern University, Department of Chemistry, the Center for Light Energy Activated Redox Processes (LEAP), and the Materials Research Center (MRC) Jacobberger, Robert; Northwestern University, Department of Chemistry, the Center for Light Energy Activated Redox Processes (LEAP), and the Materials Research Center (MRC) Huang, Wei; Northwestern University, Department of Chemistry, the Center for Light Energy Activated Redox Processes (LEAP), and the Materials Research Center (MRC) Young, Ryan; Northwestern University, Department of Chemistry, the Center for Light Energy Activated Redox Processes (LEAP), and the Materials Research Center (MRC) Pankow, Robert; Northwestern University, Department of Chemistry, the Center for Light Energy Activated Redox Processes (LEAP), and the Materials Research Center (MRC) Zhu, Weigang; Northwestern University, Department of Chemistry, the Center for Light Energy Activated Redox Processes (LEAP), and the Materials Research Center (MRC); Tianjin University School of Science, Tianjin Key Laboratory of Molecular Optoelectronic Sciences (TJ-MOS), Department of Chemistry Lu, Norman; National Taipei University of Technology, Institute of Organic and Polymeric Materials; Northwestern University, Department of Chemistry, the Center for Light Energy Activated Redox Processes (LEAP), and the Materials Research Center (MRC) Kohlstedt, Kevin; Northwestern University, Department of Chemistry, the Center for Light Energy Activated Redox Processes (LEAP), and the Materials Research Center (MRC) Sangwan, Vinod; Northwestern University, Department of Materials Science and Engineering Wasielewski, Michael; Northwestern University, Department of

	Chemistry, the Center for Light Energy Activated Redox Processes (LEAP), and the Materials Research Center (MRC) Hersam, Mark; Northwestern University, Department of Materials Science and Engineering Schatz, George; Northwestern University, Department of Chemistry, the Center for Light Energy Activated Redox Processes (LEAP), and the Materials Research Center (MRC) Delongchamp, Dean; National Institute of Standards and Technology, Material Measurement Laboratory Facchetti, Antonio; Northwestern University, Department of Chemistry and the Materials Research Center; Flexterra Corporation Marks, Tobin; Northwestern University, Department of Chemistry

ARTICLE

Non-Fullerene Acceptors with Direct and Indirect Hexa-fluorination Afford >17% Efficiency in Polymer Solar Cells

Received 00th January 20xx,
Accepted 00th January 20xx

DOI: 10.1039/x0xx00000x

Guoping Li [a,#], Liang-Wen Feng [a,#], Subhrangsu Mukherjee [b], Leighton O. Jones [a], Robert M. Jacobberger [a], Wei Huang [a], Ryan M. Young [a,*], Robert M. Pankow [a], Weigang Zhu [a,d], Norman Lu[a,f], Kevin L. Kohlstedt [a,*], Vinod K. Sangwan,[c,*] Michael R. Wasielewski [a,*], Mark C. Hersam [a,c,*], George C. Schatz [a,*], Dean M. DeLongchamp [b,*], Antonio Facchetti [a,e,*], and Tobin J. Marks [a,c,*]

The rational molecular design of non-fullerene acceptors (NFAs) in organic solar cells (OSCs) can profoundly influence photovoltaic (OPV) performance. NFA fluorination has to date proven beneficial to cell performance. However, there is a lack of comprehensive understanding of how various fluorination modalities influence film morphology, carrier mobility, molecular packing, other structural properties, electronic structure, exciton separation, and charge transport, that determine ultimate cell efficiency. Here we compare two types of end group (EG) fluorination patterns on Y6-based A-DAD-A cores, resulting in highly efficient NFAs: direct skeletal fluorination (**BTF**) and indirect trifluoromethyl fluorination (**BTFM**). These two patterns induce distinctive behaviors in the active layer blends with chlorinated donor polymer **D18-Cl** and additive, 1-chloronaphthalene, affording high PCE values of 17.30 % (**BTF** + addtive) and 17.10% (**BTFM** no-addtive) . The **BTF** vs. **BTFM** OSC performance trends can be correlated with diffraction-derived differences in molecular packing. Density functional theory (DFT) reveals remarkably low internal reorganization energies and high electronic coupling between NFA dimers, greater and more numerous than in other NFAs reported to date, thus providing extended 3D charge transport networks in the thin film crystalline domains. Transient absorption spectroscopy reveals that hole transfer from the acceptor to the donor occurs in < 300 fs and that photoexcited carriers persist for hundreds of ns in each blend film. The contrasting role of the additive in **BTF** and **BTFM** cells is further clarifieded by recombination dynamics analysis using in-situ photocurrent and impedance spectroscopy. Overall, this work provides guidance for developing new NFAs via direct and indirect fluorination strategies for high efficiency OSCs.

Broader context

Polymer solar cells (PSCs) comprised of solution processable light weight, earth-abundant, non-toxic, mechanically durable, and properties tunable organic materials offer a promising approach for large-scale/low cost light-to-electricity conversion. To date, the highest power conversion efficiencies (PCEs) near 18% have been just recently achieved with phase-separated polymer donor + small-molecule non-fullerene electron (NFA) bulk-heterojunction (BHJ) blends. However, these advances have been largely empirical with those atomistic electronic and organizational features needed to achieve optimal blend structures and exciton dynamics control only partly understood. Here, we present a detailed compare/contrast synthetic, crystallograhic, morphological, and opto-electronic analysis of the effects of two very different NFA complementary fluorination modalities in defining bulk-heterojunction organization, carrier mobility, optical cross-section and excition-splitting dynamics. The net result is PCEs well above 17% reflecting, among other factors, strong near-IR absorption, well-balanced hole and electron mobilities, as well as proper orientation of the molecular π-electron systems and compositional donor-acceptor phase separation in the PSC active layer. We also identify two NFA intermolecular interaction modes never before seen: strong F···NC bonding and bifurcated F···H-C hydrogen-bonding. The results of this study elucidate important building-block characteristics that enhance OSC performance and convey design implications for future higher performance BHJ materials.

[a.] Department of Chemistry, and the Materials Research Center (MRSEC), Northwestern University, Evanston, Illinois 60208, United States
[b.] Material Measurement Laboratory, National Institute of Standards and Technology, Gaithersburg, Maryland 20899, United States
[c.] Department of Material Science and Engineering, Northwestern University, Evanston, Illinois 60208, United States
[d.] Tianjin Key Laboratory of Molecular Optoelectronic Sciences (TJ-MOS), Department of Chemistry, School of Science, Tianjin University, Tianjin 300072, P.R. China
[e.] Flexterra Corporation, Skokie, Illinois 60077, United States
[f.] Institute of Organic and Polymeric Materials, and Research and Development Center for Smart Textile, National Taipei University of Technology, Taipei 106, Taiwan

INTRODUCTION

Solution-processable bulk-heterojunction (BHJ) organic solar cells (OSCs) offer great potential for industrialization, owing to their unique attractions of high power conversion efficiency (PCE), low-cost fabrication, light-weight, earth-

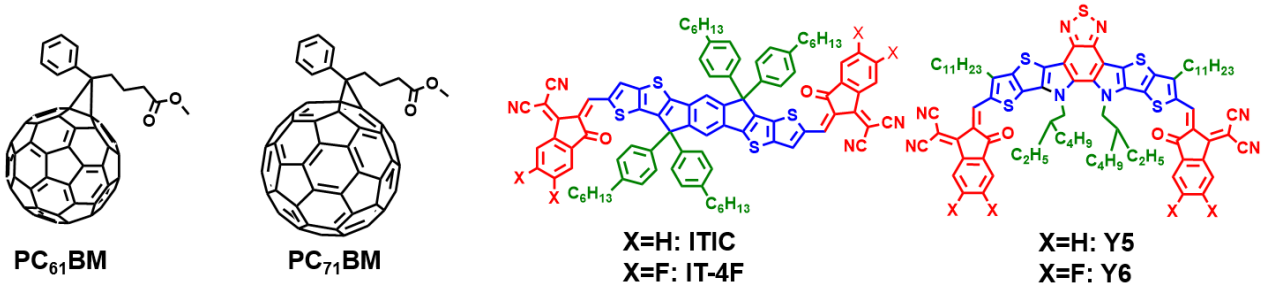

Figure 1. Examples of **a**. fullerene acceptors, **$PC_{61}BM$** and **$PC_{71}BM$** and **b.** non-fullerene acceptors, **ITIC**, **IT-4F**, **Y5** and **Y6**. Blue: electron-donating cores; Green: solubilizing sidechains; Red: electron-withdrawing moieties.

abundant materials, and nontoxic environmental footprints.[1] OSCs have thus attracted significant attention in the photovoltaic community during the past decade,[1-3] and multiple types of OSC systems have been established, such as traditional polymer donor + small molecule acceptor solar cells,[2-4] recently developed all-polymer solar cells,[5, 6] and all-small-molecule solar cells.[7] While a wealth of excellent polymer donors[8-10] have emerged, the lower power conversion efficiencies (PCEs) versus their most efficient inorganic counterparts and poor ambient/thermal stability[2, 11, 12] still a challenge for large-scale deployment.[13] These issues mainly reflect the lack of appropriate acceptor materials with matching orbital energetic and photophysical properties.[14, 15 16] In this context, compared with traditional fullerene-based acceptor ($PC_{61/71}BM$, **Figure 1a**), the recent development of non-fullerene acceptors (NFAs), with the ITIC[3, 4, 17], IT-4F[18, 19], Y5[20, 21] and Y6[22] (**Figure 1b**) as the most well-known examples, offer the promising pathways to future advances in OSC performance and technologies. Emerging, frequently empirically-derived NFAs are significantly advancing the scope and understanding of soft matter photophysical processes for light-to-electricity energy conversion, such as enabling more tunable energetics, better harnessing of near-infrared photons, and modularizing synthesis for controlled electronic structure and scale-up.

These new NFAs when matched with appropriate electron donors promote more tunable crystallinity and morphology in the blend films and therefore offer a rational route to performance increases via well-aligned energy levels, supressed recombination processes, balanced hole and electron mobilities, and increased photocurrent densities.[3, 23-27] Consequently, state-of-art OSCs are providing PCE values greater than 18% using A-DAD-A type NFAs.[28-35]The benefits of NFA tunability are illustrated by the rapid recent advances in OSCs synthetic strategies based on three main NFA components (**Figure 1b**), namely, 1) the electron-donating core, 2) the solubilizing sidechain, and 3) the electron-withdrawing end group (EG).[21] Among these strategies, the electron-withdrawing EG is considered as an essential component for creating an intramolecular "push-pull effect" to modulate intramolecular charge transfer (ICT).[36, 37] Thus, researchers have empirically explored various methods to probe the function of diverse EGs with the goal of developing superior NFAs from novel EGs.[38-42] This Laboratory and others found that EG halogenation, specifically fluorination, significantly enhances cell performance.[18, 37, 43, 44] Fluorine as the most electronegative element induces stronger intramolecular electron push-pull effects in NFAs without introducing deleterious steric impediments. Therefore, fluorinated NFAs typically exhibit more red-shifted optical absorption and lower orbital energetics, allowing them to more efficiently separate excitons at the donor - acceptor interface in the OSC bulk-heterojunction active layer.[6, 45, 46] However, fluorination strategies have so far only focused on empirical relationships between the degree of NFA F substitution and OSC performance. Specifically, there is limited understanding of how the various fluorination patterns relate to OSC performance, including the F atom steric role, the origin of distinctive NFA packing motifs, film morphological behavior, molecule-level electronic structure, and bulk photophysical properties.

Here, we report a systematic comparative investigation of the impact of two very different fluorination patterns, direct fluorination, and indirect -CF_3 fluorination, on NFA electronic, physical, molecular, morphological, and crystallographic properties. To this end we utilize the Y6 skeleton with naphthalenic π-extended EGs due to their established high photovoltaic performance,[21] and here EG modification is used as the molecular platform to implement these two distinctly different fluorination modalities. Since EG fluorine atom density strongly affects OSC performance, we introduce two fluorination patterns on benzothiazole (BT) skeleton-based NFAs, **BTF** and **BTFM**, with an identical F atom density per molecule (**Figure 2a**). **BTF** has 6 F atoms triply fluorinating the sp^2 carbons of each naphthalenic "wing"—two at the 2 and 3 positions, one distributed between the 1 and 4 positions. **BTFM** has one -CF_3 group per "wing" distributed between the 2 and 3 positions. Hence, **BTF** fluorination is directly coupled to the NFA π-system while that in **BTFM** is indirectly coupled. In both cases the isomers, differentiable by NMR, are inseparable by preparative chromatography or recrystallization (see SI Schemes S1-4 and Section 3). Comparing with benzene-based non-extended trifluorinated EG (3F-IC)[18], the naphthalene-based π-extended EG applied in this work not only facilitates intermolecular transport of the charge carriers and red-shifted the absorption[21], but it is also synthetically more cost-efficient (3F-IC: 4 steps, ~5% overall yield versus 3F/CF3-LIC: 5 steps, ~15% overall yield).

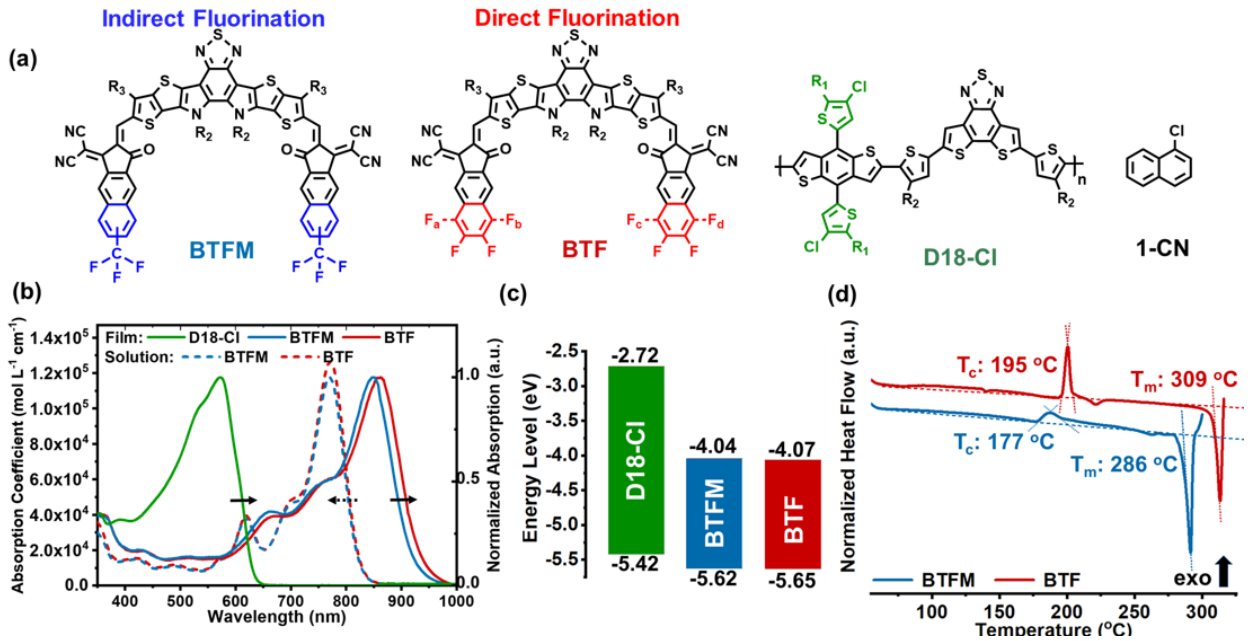

Figure 2. Structures and physical properties of the donor polymer and non-fullerene acceptors (NFAs). (a) Chemical structures of the NFAs **BTFM** and **BTF**, donor polymer **D18-Cl**, and the processing additive 1-chloronaphthalene (1-CN). R1 = 2-ethylhexyl, R2 = 2-butyloctyl, R3 = n-undecyl. For each 'wing' of **BTF**, the $F_{a\ or\ b}$= F and $F_{c\ or\ d}$ = F. (b) Optical absorption spectra of the donor and NFA film. (c) Energy levels of the D18-Cl, BTF and BTFM estimated by cyclic voltammetry (CV). (d) Frst heating DSC thermograms of the indicated solution-cast NFAs.

We focus here on a **BTF** vs **BTFM** comparative analysis with the versatile chlorinated donor polymer **D18-Cl** (**Figure 2a**).[47] While this approach surveys average contributions across each NFA structure class, properties differences are readily assignable to the two fluorination patterns. Furthermore, comparing these results with those for the non-fluorinated and EG difluorinated analogues, provides an even broader perspective-- EG trifluorination significantly red-shifts optical absorptions, compresses the optical bandgaps, and downshifts the exciton dissociation energetics – all critical for enhancing OSC performance. Precise molecular packing is first examined by single crystal X-ray diffraction, revealing for the first time a unique F-cyano group stacking motif. We also observe an unprecedented opposite OPV response of the two fluorinated NFAs to the commonly employed 1-CN processing additive. Detailed bulk-heterojunction thin-film characterization and DFT computation are also carried out. These factors together deliver enhanced device efficiency, with **BTF** blended with polymer donor **D18-Cl** yielding a maximum PCE of 17.30% *with* 0.5 % 1-CN, while the corresponding the **BTFM** blend yields a maximum PCE of 17.10% *without* 1-CN. Despite the seemingly minor differences in **BTF** vs **BTFM** PCEs, distinct disparities in OSC recombination dynamics are measured by in-situ integrated photocurrent device analysis. The favorable additive effects on **BTF** blend morphology are found to decrease bimolecular recombination and increase both carrier mobility and FF at the operating point of maximum PCE. In contrast, the presence of 1-CN in **BTFM** cells increases bimolecular recombination and depresses FF, thus providing experimental support for NFA-dependent OPV response in accord with computational results.

RESULTS AND DISCUSSION

Materials Synthesis and Physical Properties

We first describe the synthesis (Supporting Information Sections 2-3) and characterization of the new hexafluoro acceptor molecules and then discuss blends with donor polymer **D18-Cl** to probe the impact of the two trifluorination patterns on photophysical processes and photovoltaic parameters. The underlying role of two different fluorination patterns is then assessed by multiple characterization techniques, including

Table 1. Summary of acceptor optical, orbital energetic, and thermal properties.

Acceptor	λ_{max}^{sol} (nm)	λ_{max}^{film} (nm)	$\Delta\lambda_{max}$ (nm)	λ_{onset}^{opt} (nm)	E_g^{opt} (eV)	$E_{HOMO/LUMO}^{CV}$ (eV)	E_{HOMO}^{UPS} (eV)	$T_{C,onset}$ (°C)	ΔH (J/g)	$T_{m,onset}$ (°C)	ΔH_{fusion} (J/g)
BTF	772	863	91	948	1.31	-5.65/-4.07	-5.61	195	8.3	309	15.9
BTFM	772	849	77	935	1.33	-5.62/-4.04	-5.58	177	3.2	286	19.6

single-crystal x-ray diffraction (XRD), density functional theory (DFT) level computation, space-charge-limited current (SCLC) measurements, 2D-grazing incidence wide angle X-ray scattering (2D-GIWAXS), AFM, TEM, and impedance-based integrated photocurrent device analysis (IPDA). All experimental details are placed in the Supporting Information (SI). The synthetic pathways to the two new NFAs are outlined in SI Schemes 1-4. ^{1}H, ^{13}C, ^{19}F NMR spectra and mass spectra are also provided in the SI (**Figures S1-31**). The thermal properties of the two NFAs were studied by TGA and DSC. TGA shows that both the acceptors possess thermal decomposition temperatures above 300 °C (5% mass loss, **BTF**: 328 °C, **BTFM** 301 °C (**Figure S35**), suggesting good thermal stability.

The UV-visible optical absorption spectra of **BTF** and **BTFM** are shown in **Figures 2b** and **S32,** and data are summarized in **Table 1**. In dilute $CHCl_3$ solution, the spectra of **BTF** and **BTFM** are nearly identical with the maximum (λ_{max}^{sol}) and shoulder peak located at 772 nm and 697 nm, respectively, indicating that both fluorination patterns are equally effective in creating NFA ICT effects. Furthermore, nearly identical 0-1 and 0-0 peak intensity ratios[48] for **BTF** and **BTFM** suggest nearly equal strength in intramolecular electron push-pull effects. The slightly higher absorption coefficient found for **BTF** solutions (1.28×10^5 mol L^{-1} cm^{-1} at λ_{max}^{sol}) vs **BTFM** solutions (1.17×10^5 mol L^{-1} cm^{-1} at λ_{max}^{sol}), presumably reflects the direct F - C_{sp2} p-π interaction in the former chromophore. For spin-coated films, both NFA spectra are strongly red-shifted, indicating the existence of J-like aggregation. However, **BTF** is more red-shifted than **BTFM** (**Table 1**), indicating a greater extent of close intermolecular stacking which is supported by the x-ray diffraction results (*vide infra*). Furthermore, the impact of the two fluorination patterns can be seen in the onset of film optical absorption, 948 nm for **BTF** vs 935 nm for **BTFM** ($\Delta\lambda_{max}$ = 91 vs. 77 nm), arguing that direct ring fluorination is more effective here in narrowing the energy bandgap.

We next estimated the LUMO and HOMO energy levels by cyclic voltammetry (CV; using the usual approximations,[49, 50] **Figure S33**) and ultraviolet photoelectron spectroscopy (UPS, **Figure S34**). The **BTF** HOMO level is, CV: -5.65eV, UPS: -5.61 eV, and lies slightly lower than that of BTFM, CV: -5.62 eV, UPS: -5.58 eV. The **BTF** LUMO level, CV: -4.07 eV, is also lower than that of **BTFM**, CV: -4.04 eV.

Regarding thermal properties, DSC was also employed to study the thermal behavior of the neat **BTF** and **BTFM** acceptors (**Figure 2d**). Note that **BTF** shows a higher crystallization-transition temperature (T_c, **Table 1**) and normalized crystallization-transition enthalpy (ΔH_C, **Table 1**) than **BTFM**, suggesting that the former has greater lattice cohesion and a higher tendency for crystallization and aggregation than the latter.[51, 52] This suggests a more extended acceptor domain in the **BTF**-derived D-A blend film active layer (*vide infra*). Both the acceptors begin to decompose immediately after the endothermic melting process is complete and the decomposition temperatures are in good agreement with the aforementioned TGA data (*vide supra* and **SI Section 8**).

Photovoltaic Characteristics and Carrier Mobility

Next the comparative photovoltaic performance in a conventional OSC architecture, ITO-glass/Hole transport layer/Donor: Acceptor BHJ active layer /Electron transport layer/Ag, was probed. Optimization of the fabrication process is described in SI Section 9. The **D18-Cl:BTF**-based devices show a slightly lower V_{OC} of ≈0.86 V vs the **D18-Cl:BTFM**-based devices (V_{OC} ≈0.88 V), in agreement with experimental energy levels (**Figure 2b; Table 2**). Note that the energy loss, $\Delta E_{loss} = E_g^{opt} - q*V_{OC}$, where E_g^{opt} is the optical bandgap, and q the unit charge, of both acceptors is as low as 0.45 V, which is in the cohort of the most efficient NFAs reported to date.[53, 54] Similar values of ΔE_{loss} for these two acceptors argues that the two fluorination modalities similarly impact OSC performance in terms of how they affect exciton dissipation pathways. However, compared with the **BTFM**, the **BTF**-based devices produce a slightly higher short circuit current density (J_{SC} = 27.1 *vs*. 26.4 mA cm^{-2}) in accord with the slightly red-shifted **BTF** absorption edge.

Interestingly, the **D18-Cl:BTF**- and **D18-Cl:BTFM**-based OSCs show opposite responses to the 1-CN processing additive (**Table 2**). Compared with the latter that achieve a higher PCE without 1-CN, the former devices require 1-CN for optimum performance. Thus, OSC performance was optimized to achieve a state-of-the-art PCE = 17.3% in **D18-Cl:BTF** devices with 0.5% 1-CN while a PCE = 17.1% in **D18-Cl:BTFM** devices with no processing agent (1-CN depresses performance). In general, processing additives are known to enhance the FF contribution to OSC performance,[55, 56] and therefore, we hypothesize that the aromatic 1-CN additive favorably influences film morphology by interacting with the acceptor aromatic π-expanse.[57, 58] To support this hypothesis, we investigated another effective processing additive, 1,8-diiodooctane (DIO), which has an aliphatic chain with no π-electron structure.[59-61]

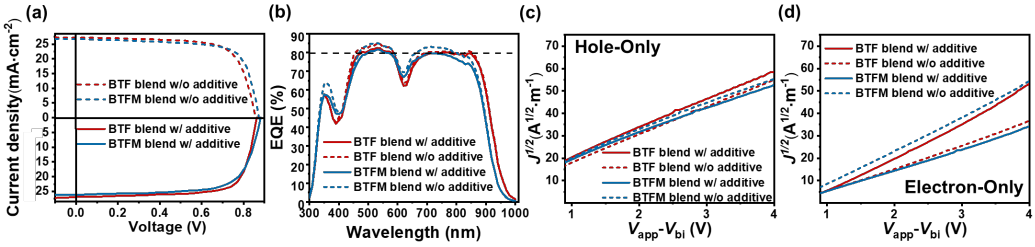

Figure 3. Photovoltaic properties and carrier mobilities of D18-Cl:NFA OSCs. (a) OSC current-voltage (J-V) characteristics;(b) Corresponding external quantum efficiency (EQE) data for the indicated the blends; (c) Hole-only and (d) electron-only mobilities measured by SCLC.

Table 2. Summary of the photovoltaic performance parameters and charge carrier mobilities for the indicated OSC blends.

Blend (D18-Cl)	V_{OC} (V)	J_{SC} (mA cm^{-2})	$J_{SC}^{cal, b}$ (mA cm^{-2})	FF (%)	PCE [c] (%)	μ_h (*10^{-4} cm^2 V^{-1} s^{-1})	μ_e (*10^{-4} cm^2 V^{-1} s^{-1})	μ_h /μ_e
BTF	0.860	27.19	26.67	72.05	16.83 (16.13±0.58)	2.08±0.33	1.71±0.22	1.21
BTF [a]	0.863	26.87	26.23	74.57	17.30 (16.77±0.53)	1.87±0.24	0.99±0.42	1.89
BTFM	0.875	26.72	26.31	73.12	17.10 (16.38±0.62)	1.35±0.32	0.95±0.18	1.42
BTFM [a]	0.882	26.18	25.28	70.62	16.27 (15.82±0.42)	1.51±0.43	1.43±0.25	1.37

[a] Fabricated with 1-CN as processing additive. [b] J_{SC} ^{cal} is calculated from the integration of the external quantum efficiency spectrum. [c] Photovoltaic data reported as averages taken over 10 separate devices where ± represents one standard deviation of the mean.

In the present case, replacing 1-CN with DIO (SI Section 9) lowers the performance of both the **D18-Cl:BTF** and **D18-Cl:BTFM** devices, mainly by reducing the FF and J_{SC}. These results support the hypothesis that the 1-CN π-electron system plays a specific role in controlling blend film morphology and thus influences the device performance. A similar tendency is argued from thin-film characterization and DFT computation (*vide infra*).

Next assessed were hole and electron mobilities in hole-only and electron-only devices (device fabrication details are in SI Section 12) using the SCLC method **(Figure 3b**, **Table 2**, and **Figure S45**). Interestingly, the hole mobility of the **D18-Cl:**NFA blend films, which is dominated by the donor domains, is not significantly impacted by the 1-CN additive (**D18-Cl:BTF**, 2.08 *vs*. 1.87; **D18-Cl:BTFM**, 1.35 *vs*. 1.51; in units of *10^{-4} cm^2 V^{-1} s^{-1}). However, electron mobility, dominated by the acceptor domains, is significantly altered upon 1-CN addition (**D18-Cl:BTF**, 1.71 *vs*. 0.99; **D18-Cl:BTFM**, 0.95 *vs*. 1.43; in units of *10^{-4} cm^2 V^{-1} s^{-1}). These mobility variations correlate well with relative device performance, and further support the hypothesis that the 1-CN additive mainly influences the acceptor domains of the BHJ active layer.

Molecular Packing and Crystallographic Analysis

To understand the relationship between the two different fluorination methods and the intermolecular packing, diffraction-quality single crystals of the **BTF** and **BTFM** were grown from saturated halogenated solvents. Multiple diffraction experiments were carried out on different samples in attempts to achieve the lowest goodness of fit (GooF) which are reported here (**SI Section 9**). In the single-crystal analysis of **BTF**, all three isomers co-crystallize in the unit cell of the refined **BTF** structure. So, it can be inferred that the three **BTF** isomers possess very similar crystallization characteristics. In contrast, even after multiple crystal growing attempts under different

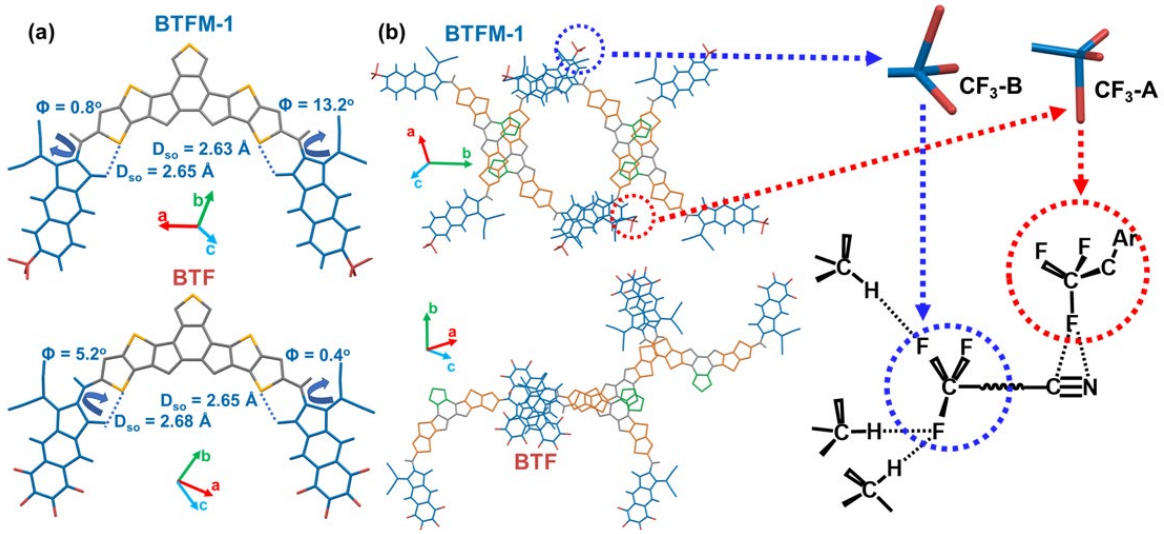

Figure 4. Single-crystal structures the present NFAs. (a) Plan view of the **BTFM** and **BTF** molecular conformations, where D_{so} = the distance of the S···O interactions, Φ = the core - end group twist angle through the vinyl connection. **(b) BTFM** and **BTF** stacking motifs viewed along the EG stacking direction. The colors indicate different NFA components: red = F and CF_3 group; blue: = naphthalenic end group; yellow = thieno[3,2-b]thiophene core unit; green = thiadiazole core unit; and the drawing illustrates the spatial orientation of the F···CN interaction and the two types of F···H-C hydrogen bonds.

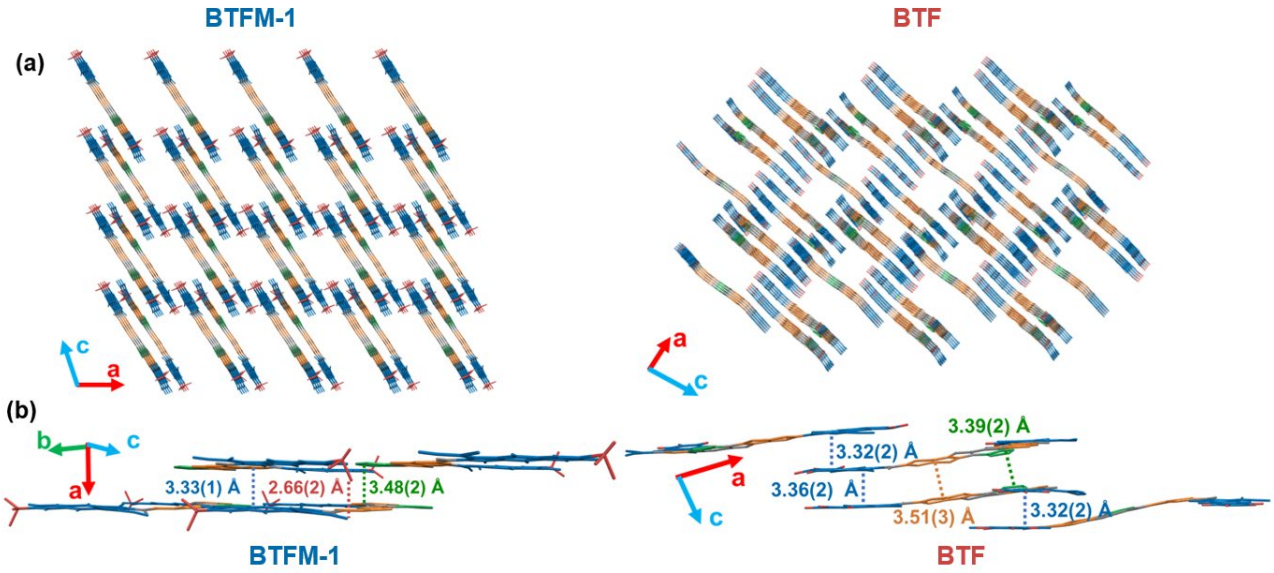

Figure 5. Single Crystal molecular packing and the stacking distance of the present NFAs. (a) Long-range stacking pattern viewed along the b-axis. **(b)** NFA molecule crystalgraphic π-π stacking distances in the single crystal.

conditions, only a single isomer of **BTFM** could be crystallized (named, **BTFM-1, SI Scheme S4**) as seen in the refined crystal structure (**Figure 4a**). From the bulk material solution NMR, **BTFM-1** only accounts for ~25% of the total composition of **BTFM**, suggesting the **BTFM-1** may possess a higher crystallinity or a lower solubility than the other two isomers, such that **BTFM-1** crystallizes first from the supersaturated solution.

Generally, both acceptor molecules exhibit crescent-like configurations enforced by short sulphur-oxygen interactions, acting as conformational locks (Dso, **Figure 4a**).[62, 63] noticeably smaller intramolecular torsion angle than does **BTFM-1** (Φ = 5.2° vs. 13.2°, **Figure 4a**), which provides greater planarity for **BTF**, and thus is able to accommodate more electronic coupling to neighbours (*vide infra*). The two different fluorination modalities also induce differences in inter-molecular stacking. **BTF** exhibits diverse EG-EG stacking interactions (**Figure 4b**, blue) compared with **BTFM-1**. Besides the EG-EG stacking, **BTF** also has stacking between two thieno[3,2-b]thiopene units (TT-TT, **Figure 4b**, yellow) and two benzothiazole units (BT-BT, **Figure 4b**, green). In the case of **BTFM-1**, the TT-TT and BT-BT stacking motifs are absent, however two TT-BT stackings are observed. Surprisingly, it can be seen that one of the two trifluoromethyl groups (CF3-A, **Figure 4a-b**) participates in the intermolecular EG-EG stacking of **BTFM-1** (**Figure 4b**, red circle) with a close F···N cyano group interaction (~2.66 Å).[64] Also, the cyano group C≡N bond length is impacted by donating a sigma hole to form a F-π interaction with CF_3-A (**Table S4**).[65] Compared with **BTF**, this unique CF_3-assisted stacking not only increases the electronic coupling strength in **BTFM-1** stacking (72 meV vs. 26 meV, *vide infra*), but also establishes bifurcated hydrogen bonds[66-68] between a F atom on CF_3-B and the proton on the N-alkyl chain (**Figure S36, Table S4**).[65] This EG to alkyl chain hydrogen bonding therefore limits the free rotation of the N-alkyl chain. Interestingly, when the consecutiveness of **BTF** and **BTFM-1** stacking motifs is examined, it is seen that only the EG-EG stackings propagate through the entire crystal network (**Figure 5a**, blue), while other types of stacking (TT-TT, BT-BT, and TT-BT) are all localized and separated spatially (**Figure 5a**), which suggests that the main charge transport is indeed through the EG-EG stackings.

The repeat distances of all the stacking motifs in the crystal networks of **BTF** and **BTFM-1** were also calculated, including estimated standard deviations (**Figure 5b**) to analyze the crystallization differences induced by these two molecular level fluorination patterns. Compared with the previously reported single-crystal structures of non-fluorinated **Y5** and **BT-LIC,**[21] both of the present newly developed acceptors have closer EG-EG stacking distances of ≈ 3.34 Å. This close EG-EG stacking in **BTF** and **BTFM-1** no doubt facilitates electron transport without sacrificing the solution processibility, and thus enhances the bulk carrier mobilities. That the corresponding OSCs with direct and indirect fluorination both exhibit superior performance metrics is not completely surprising.

Computational Studies

We begin with computation of the frontier molecular orbitals (FMOs) of the subject NFAs. The HOMO energies are -5.76 eV for both **BTFM-1** and **BTF**, across all isomers (Supporting Information, **Figures S62**, **S64-S75**) and are in reasonable agreement with cyclic voltammetry and ultraviolet photoelectron spectroscopy (**Table 1**); likewise, the lowest unoccupied molecular orbital (LUMO) energies are around -3.79 eV across all structures. Their HOMO-LUMO gaps are on average 1.97 eV. These energies are in good agreement with those of the previously reported BT series of NFAs.[40, 46]

The internal reorganization energies (IREs) were then computed using the four-point method[69] (SI, Section 16); see full details in **Table S16**. The electron IREs are smaller than those

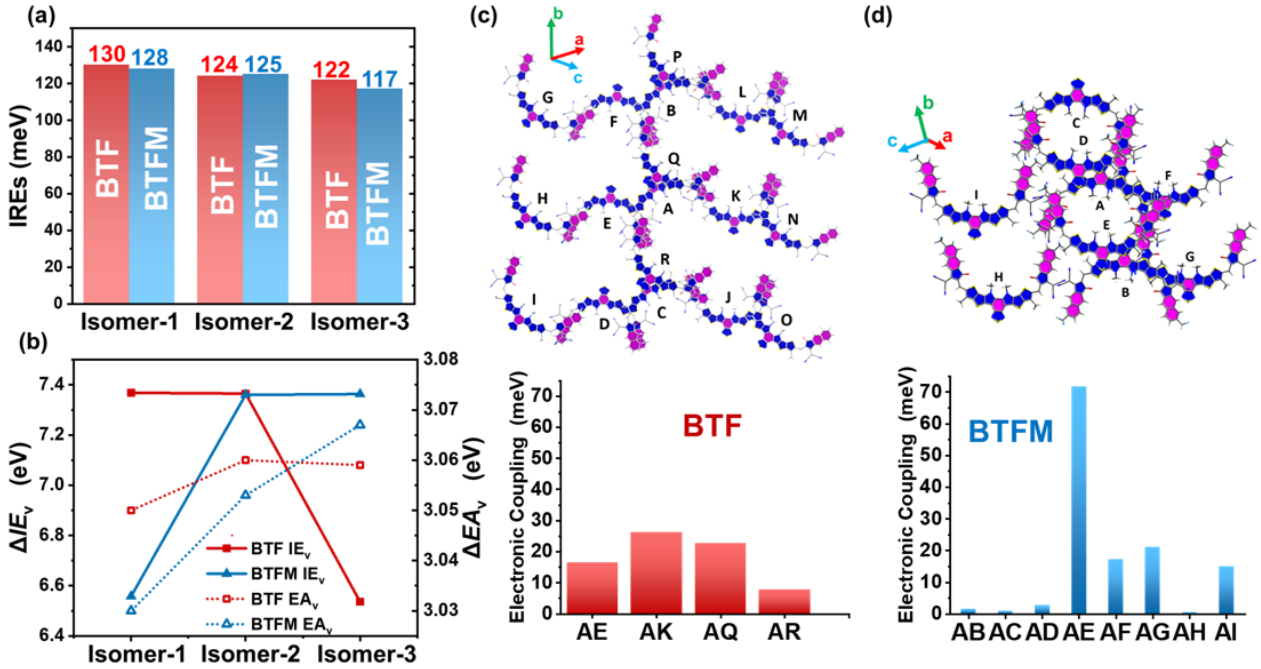

Figure 6. Summary of the NFA computational results. (a) Computed internal reorganization energies (IREs, λ_e) of the isomers of the **BTF** and **BTFM**. **(b)** Vertical ionization energy (ΔIE_v) and vertical electron affinity (ΔEA_v) of **BTF** and **BTFM**. Computed electronic coupling within the **(c) BTF's** and **(d) BTFM-1's** crystal networks (top) and the plot of coupling strengths (bottom), the letters indicate each individual coupling neighbor. Note that only the pairs with nonzero coupling strength are plotted.

in our previously reported difluorinated **BT-BO-L4F** and **Y6** molecules,[46] suggesting enhanced facility of electron transport. This is in agreement with the significantly higher vertical electron affinities (≈ 3.05 eV) vs the BT series, by 0.1-0.2 eV; adiabatic affinities are also provided and act as a measure of the NFA stability towards a trapped/localized electrons, such as a relaxed anion state, and are ≈3.07-3.21 eV. Interestingly, as more F atoms point 'inside' (from isomer-1 to isomer-3, SI Scheme S3), the IREs show a decreasing tendency in both BTF and **BTFM-1**, whereas the vertical electron affinities show an increasing tendency (from isomer-1 to isomer-3, SI, Scheme S4). This suggests that the 'inside' Fs may be more effective in reducing bimolecular recombination while the 'outside' Fs tend to stabilize excitons. **Figures 6c-d** show the electronic coupling between the near-neighbor pairs[70] of each dimer relative to a central molecular structure, in each single crystal of **BTFM-1** and **BTF**. The **BTF** crystal has up to 17 near-neighbors, while non-zero coupling exists for only four dimers, which range between 7.76 and 26.17 meV. That said, four appreciable electronic couplings are unusual, as only two normally exist.[21, 50] The **BTFM-1** crystal has eight near-neighbors, all with non-zero coupling; full details are summarized in **Table S18** and **Figure S63**. Three dimers have appreciable electron-coupling (AF: 17.11 meV, AG: 20.96 meV, AI: 14.91 meV) while a fourth has significant electron-coupling (AE: 71.56 meV). The fact that both **BTF** and **BTFM-1** have more than two electron transport pathways is consistent with the higher-performing PCEs than in previous NFA structures, but may not be the exclusive origin.[43]

The frontier molecular orbitals (FMOs) were visualized for the dimer pairs with appreciable coupling and are shown in **Figures S63-S74**. We see that in those dimers with EG-EG overlap, the LUMO density is delocalized between the two EGs of each pair, while their HOMOs are not. For core-core overlap, such as with the **BTFM-1** dimer AD, the HOMO density is delocalized across the structures in the pair. This is further evidence that the end groups of the NFAs are key to the electron transport.[70]

Morphological Characterization

To understand how the two types of fluorination modalities impact the film morphology and crystallinity of the BHJ films, the donor-acceptor blend films were characterized with AFM, high-resolution TEM, 2D-GIWAXS, and Resonant Soft X-ray Scattering (RSoXS). The surface roughness of the blend films was first imaged by AFM. Both the **D18-Cl:BTF** and **D18-Cl:BTFM** films exhibit smooth surface features within the imaging area (RMS < 1 nm, 200 nm × 200 nm, Figure 7, SI Figures S39-S41.) and have similar surface roughness when processed similarly (Rq ≈ 0.6 nm without the 1-CN additive; Rq ≈ 0.8 nm with additive), suggesting that the different NFA fluorination patterns do not significantly alter the D-A phase microstructure. Upon addition of the 1-CN additive to the donor + acceptor solutions, both the blend films slightly increase in surface roughness.

To further understand how the two types of fluorination and the additive affect the phase separation of the blend films, TEM images were recorded in the bright field mode (SI Section 13), in which the more crystalline or denser acceptor domains more strongly scatter electrons,[46, 71] and thus appear to be darker in the images[72] (**Figure 7**). When there is no additive in the blend films, the **BTF** blend shows

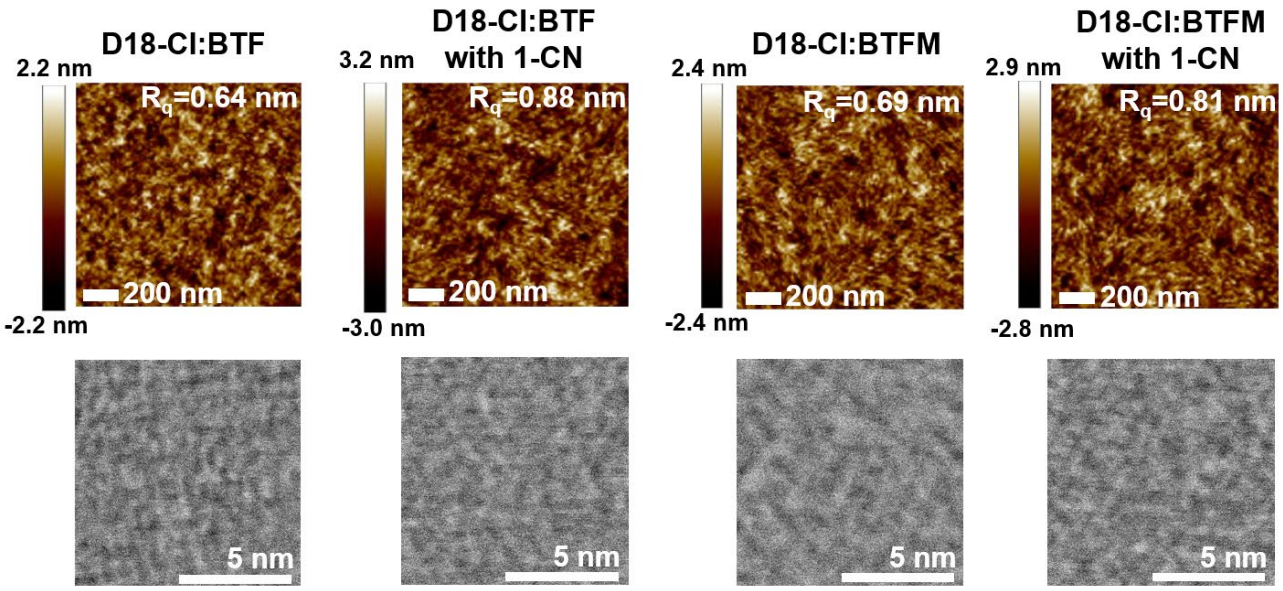

Figure 7. TEM and AFM images of D18-Cl:BTF and D18-Cl:BTFM blend films. First row: AFM height images oblend surfaces Second row: TEM images of blend films, where the darker region stands for acceptor aggregation features of the blend films.

a greater volume fraction of dense regions compared to the **BTFM** blend. This suggests that **BTF** naturally possesses greater crystallinity than **BTFM**, consistent with the UV-Vis, DSC, and GIWAXS crystallinity trends noted above and below. Interestingly, upon the addition of 1-CN to the **BTF** blend (0.5% v/v, the molar 1-CN :NFA mole ratio in the coating solution ≈ 10:1), fewer dense regions appear suggesting that the crystallinity of the **BTF** in the blend film is reduced. In **BTFM**, the 1-CN additive leads to a larger volume of dense regions, suggesting the crystallinity of **BTFM** was enhanced. To further understand the impact of fluorination and additive on the film morphology, the blend films with 3% 1-CN additive and without additive were both next characterized by 2-D GIWAXS and RSoXS combining with simulated (from the single-crystal analyses) powder x-ray diffraction patterns to investigate the differences in packing and ordering caused by the different fluorination patterns and the additive.

The 2-D GIWAXS patterns, pole **Figures**, relative crystallinities, in-plane and out-of-plane 1-D profiles, and the d-spacings of the blends are summarized in **Figures 8a-c**, **S46-48** and **Tables S12-S13**. Importantly, strong low-q peaks in the range 0.35 – 0.5 $Å^{-1}$ are observed in both neat acceptor and blend films and likely arise from acceptor ordering, but these peaks are absent in the single crystal diffraction data of the neat acceptors. Therefore, GIWAXS reveals that instead thin film polymorphs of the small molecule acceptors are present with a unit cell that was not observed in the single crystals. For consistency, attempts to index the peaks of these polymorphs by analogy to the single-crystal indexing were made.

In the neat films of both acceptors, an (h00) π-π stacking peak (crudely analogous to the *a*-axis of the single-crystal unit cells) appears at ≈ 1.7 $Å^{-1}$ with a strong out-of-plane preference, as shown in the 2-D data as well as the pole Figures, suggesting that the molecules both exhibit a preferential π-face-on orientation of the conjugated plane.[6, 73, 74] The intermolecular d-spacing of the two acceptors calculated from the (h00) π-π stacking peak is observably different (**BTF** ≈ 0.35 nm, **BTFM** ≈ 0.37 nm) suggesting a closer stacking distance in the ring-fluorinated acceptor, **BTF**, which is consistent with the trend found in the single-crystal structures (*vide supra*).

The 2-D GIWAXS data for the blend films are shown in **Figure 8a**. In all four blend films and the corresponding neat films, a characteristic (00l, q_{xy}) reflection located at ≈ 0.32 $Å^{-1}$ can be assigned to the alkyl-chain lamellar periodicity of the **D18-Cl** (crudely analogous to the c-axis of the single-crystal unit cells). This suggests the preferential π-face-on ordering characteristics of the donor are mostly retained in the blend film. For a consistent comparison, the relative degree of crystallinity (rDoC) of the blend films (**Figure. 8c**) was calculated from the predominantly out-of-plane π-π (h00) peak near 1.7 $Å^{-1}$, which the GIXD patterns for both molecules exhibit. The rDoC is seen to decrease with 1-CN addition in the **D18-Cl**:**BTF** blend whereas in the **D18-Cl**:**BTFM** blend addition of 1-CN results in a slight increase of film crystallinity. Similar trends among the blend systems are also seen when rDoC is calculated using the low-q peaks over the range 0.3 to 0.5 $Å^{-1}$ (**Figure. S47**). When the 1-CN was added to the blend film, the d-spacings corresponding to the low-q peaks in the above range from both the **D18-Cl**:**BTFM** and **D18-Cl**:**BTF** films increase monotonically.

The diffraction coherence length (CL) as measured using a Scherrer-style analysis[75] shows the opposite trend in the **D18-Cl**:**BTF** and **D18-Cl**:**BTFM** blends. In the (h00) direction, compared with the undoped film, the CL from the low-q peaks corresponding to acceptor ordering in the 1-CN doped **D18-Cl**:**BTFM** blend film increase from 9.0 nm to 20.9 nm, indicating the formation of larger crystalline acceptor domains. But the CL of the corresponding peak from the 1-CN doped **D18-Cl**:**BTF**

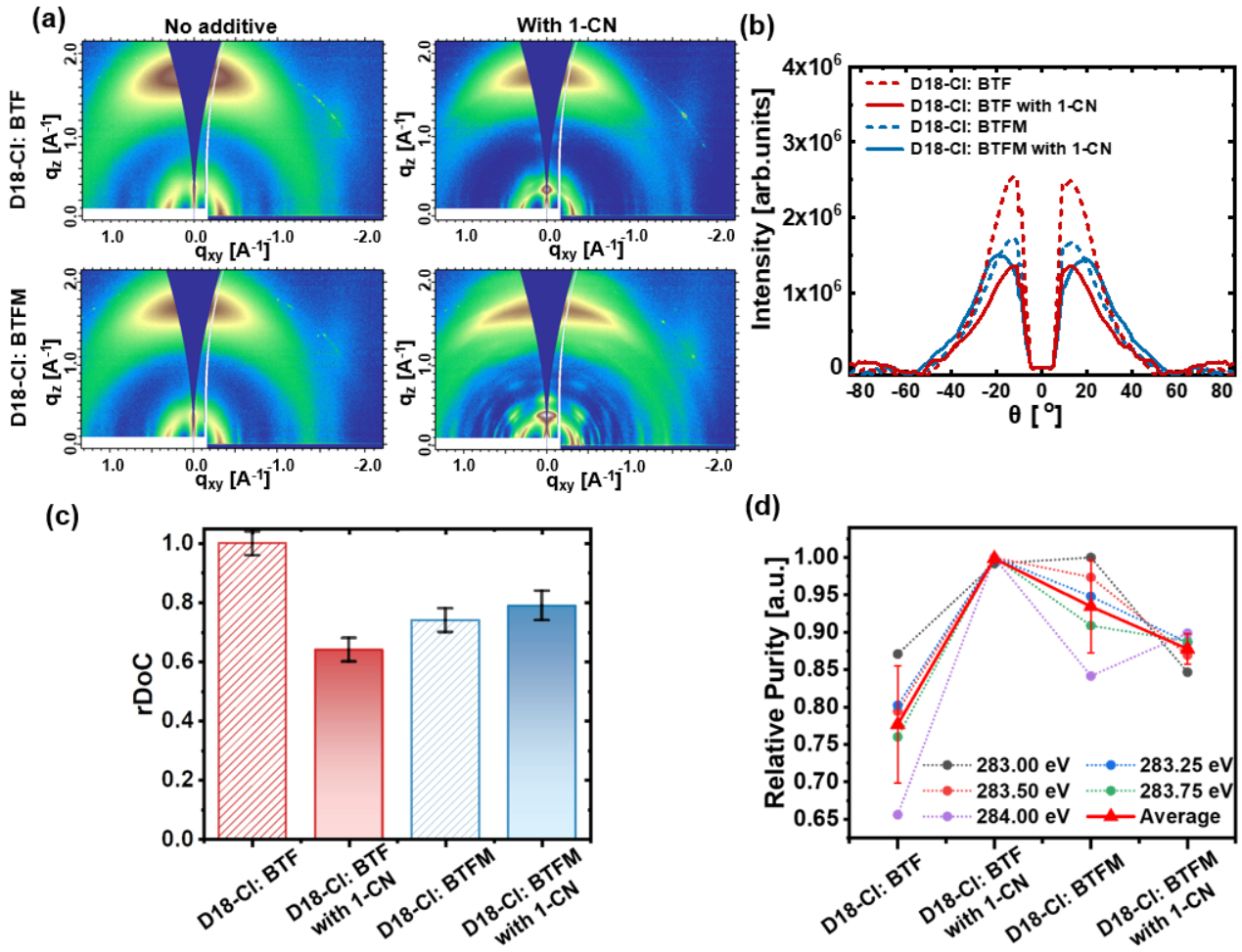

Figure 8. X-ray characterization of D18-Cl:BTF and **D18-Cl:BTFM blends and relative blend film domain purity. (a)** 2-D GIWAXS patterns. **(b)** pole figures calculated from (h00) π-π stacking peak at 1.7 Å^{-1}. **(c)** plot of relative degree of crystallinity of the 4 blends obtained by integrating the pole figures in (b). **(d)** Relative average phase purities from R-SoXS. The purity uncertainties calculated from R-SoXS data were acquired at photon energies in the range of 283−284 eV.

blend film decreases from 12.6 nm to 5.7 nm, indicating the acceptor domain size along this axis was suppressed by the 1-CN additive. This result is also consistent with the overall decrease in rDOC of **D18-Cl**:**BTF** with 1-CN addition. For the (h00) π stacking peak, the CL of both the **D18-Cl**:**BTFM** and **D18-Cl**:**BTF** blends increase by different extents by the 1-CN additive (**D18-Cl**:**BTFM**: 2.4 to 7.0 nm, **D18-Cl**:**BTF**: 2.4 to 4.8 nm).

The RSoXS analysis (**Figures 8d** and **S48**) indicates that all samples show higher scattering intensity in low-q at resonant and non-resonant energies implying that this feature likely arises from large scale (> 100 nm) mass roughness variations.[49, 76] Samples with 1-CN exhibit a slightly higher intensity of this low-q peak (also in non-resonant 270 eV profiles) indicating a slightly coarser morphology with 1-CN addition that is consistent with the surface features found in AFM. The four sets of films exhibit a close sample domain purity distribution, but from the overall trend derived from the averages of the different scattering energies, it can still be seen that the 1-CN imparts an opposite effect on the domain purities (estimated by orientation contrast contribution at different energies) for the **D18-Cl**:**BTF** and **D18-Cl**:**BTFM** blends which is consistent with the observations from HR-TEM above.

Femtosecond Transient Absorption Spectroscopy

Femtosecond (fsTA) and nanosecond (nsTA) transient absorption spectroscopy were conducted to explore the dynamics of charge separation and recombination in the donor/acceptor bulk heterojunction films. The films were pumped with a laser pulse at 830 nm and the transient absorption was detected using a broadband white light source. The 830 nm pump is near the peak absorption of the **BTF** and **BTFM** acceptors and is in a spectral region where absorption of the **D18-Cl** donor is negligible. Therefore, the regions of **BTF** and **BTFM** within the bulk-heterojunction films are selectively photoexcited, enabling exciton generation/diffusion in the acceptor and hole transfer from the acceptor to donor while suppressing exciton generation/diffusion in the donor and

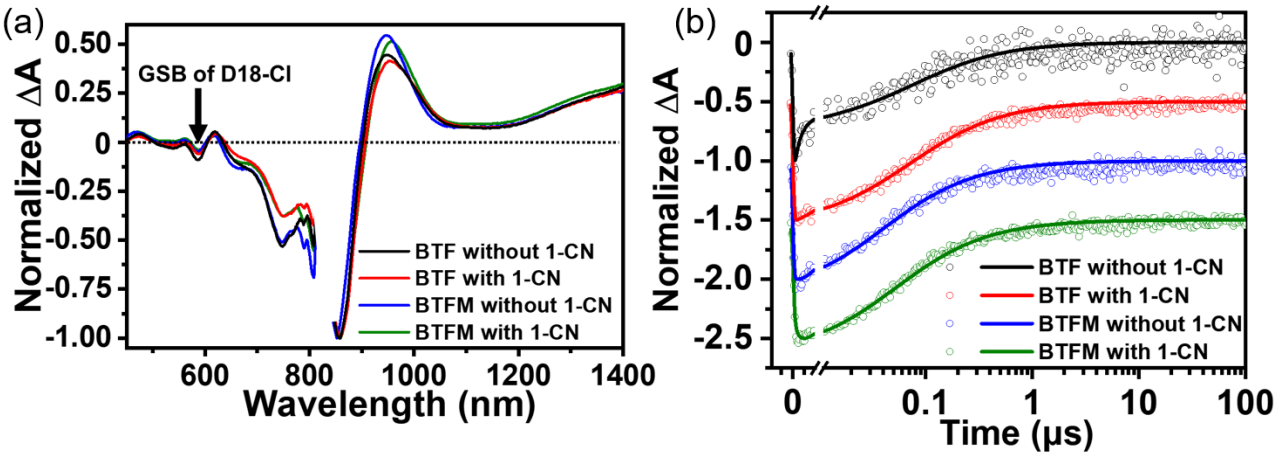

Figure 9. (a) Evolution-associated spectra of the first species that is detected within the instrument response time of ≈300 fs for **D18-Cl**:**BTF** and **D18-Cl**:**BTFM** blend films. **(b)** Kinetics (circles) and corresponding fits (lines) of the ground-state bleach of the **D18-Cl** polymer obtained from nsTA. Plots are offset vertically by 0.5 for clarity. The films are excited at 830 nm.

electron transfer from the donor to acceptor and precluding energy transfer. The kinetics are fit via global analysis using a sequential A → B → C → D model, as described further in the SI, **Figures S50-S61**, and Tables S14-S15, in which the last term is quadratic to account for bimolecular recombination of the free carriers.

Since the ground-state bleach of **D18-Cl** at ≈590 nm is within the instrument response time of ≈300 fs in fsTA, we infer an ultrafast exciton generation process in the **BTF** and **BTFM** acceptors in the blends, and ultrafast hole transfer from the **BTF** and **BTFM** acceptors to the **D18-Cl** donor. (**Figure 9a**). The profile spectra observed within the instrument response for each of the four blend films are similar, suggesting the OSC performance difference is less likely caused by the photo-excitation and hole transfer processes occurring within these early stages. Instead, the data are consistent with our hypothesis that different electron transfer processes induced by the different BHJ morphologies in the acceptor domains causes the performance difference in the devices. The kinetics of the ground-state bleach of **D18-Cl** (**Figure 9b**) indicate that free carriers persist for hundreds of ns in each of the blend films, ensuring the effective transport of the charge carriers. The ground-state bleach of **D18-Cl** is depleted by 90% within 470, 680, 420, and 550 ns for films containing **BTF** without 1-CN, **BTF** + 1-CN, **BTFM** without 1-CN, and **BTFM** + 1-CN, respectively. This tendency suggests that the lifetime of free carriers in each of the blend films is generally similar, although free carriers live longer in films with the 1-CN additive.

Charge Recombination and Extraction Dynamics

To further elucidate the roles of the two fluorination modalities in the present photophysical processes, we performed in-situ measurements of recombination dynamics of photoexcited carriers in fully functional cells. To this end, we performed integrated photocurrent device analysis (IPDA)[43, 46, 77] in the **D18-Cl**:**BTF** and **D18-Cl**:**BTFM** devices with and without 1-CN additive (0.5%) in an N_2 glove box. The motivation for developing IPDA is because it gives a more accurate value for relevant OSC parameters, especially recombination coefficient (k_{br}) compared to conventional methods such as open-circuit voltage decay (OCVD).[77] In-situ IPDA measurements in the inert environment, for the first time, allowed us to reveal minor differences in the recombination parameters in high-performance NFA OSCs having PCE differences of less than 1% (PCE >17%). Earlier, ambient IPDA measurements could only reveal underlying photophysical processes in OSCs with dramatic differences in cell performance originating from EG functionalization or annealing conditions.[46, 49, 78] Since, additives in OSCs improve performance via increased FF, bimolecular recombination related losses are expected to differ in cells with and without the additive. As described elsewhere,[77] IPDA quantifies both recombination rate (k_{br}) and charge extraction rate (k_{ext}) through in-situ measurement of carrier lifetime and mobility at the maximum power point ($V = V_{mp}$). These parameters are extracted from photocurrent and chemical capacitance measurements via impedance spectroscopy as a function of bias and illumination intensity while total number of carriers ($n = n_{mp}$) at $V = V_{mp}$ are calculated from a self-consistent iterative method. **BTF** devices (SI **Figures S76-77**) with 1-CN additive show a roughly two-fold smaller value of average k_{br} at a larger average n_{mp} value compared to **BTF** devices without the additive (**Figure 10a**). In contrast, **BTFM** devices with 1-CN additive show a reduced recombination rate at a larger n_{mp} value compared to **BTFM** cells without the additive. Likewise, the average mobility of electrons and holes, charge extraction, and charge recombination lifetime show similar trends between the two kinds of cells (**Figures 10b, c**). Overall, the FF in OSCs using fullerenes, NFAs, and poly-small-molecule acceptors is known to correlate with these parameters through a competition factor ($\theta \sim k_{br}/k_{ext}$) that takes into account competing charge extraction and recombination processes.[79] Overall, the **D18-Cl**:**BTF** OSCs with additive have a larger FF and smaller θ than **D18-Cl**:**BTF** cells without additive (**Figure 10d**). However, **D18-Cl**:**BTFM** cells with additive show a smaller FF and larger θ compared to **D18-Cl**:**BTFM** cells without the additive. The differences in average values are clearly evident despite significant device-to-device variations between kind of

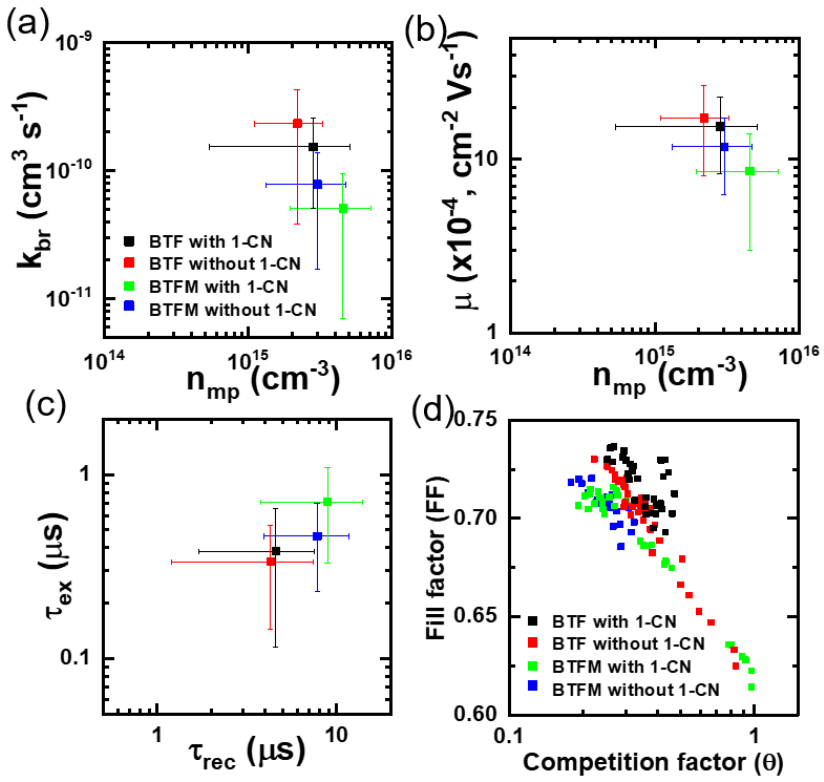

Figure 10. **(a)** Plot of average in-situ bimolecular recombination coefficient (k_{br}) versus average carrier density (n_{mp}) at maximum power point for **D18-Cl:BTF** and **D18-Cl:BTFM** cells with and without 1-CN additive. The data is averaged over 4-6 cells of each kind and error bars show standard deviation. **(b)** Average of In-situ carrier mobility (μ) versus average nmp for the four kinds of solar cells shown by the legend in (a). **(c)** Plot of average charge extraction time (τ_{ex}) versus average recombination lifetime (τ_{rec}) for the solar cells shown by legend in (a). **(d)** Fill factor (FF) versus competition factor (θ) for total 21 devices measured for **D18-Cl:BTF** and **D18-Cl:BTFM** cells with and without the 1-CN additive. Data for all 5 different illumination intensities from 0.3 Sun to 1.0 Sun are included.

cell (**Figures 10a-c**), highlighting the robustness of the analysis. Thus, the inverse relation between FF and θ can be directly correlated with improved blend morphology in the **D18-Cl**:**BTF** cells with 1-CN additive and **D18-Cl**:**BTFM** cells without the additive, as suggested by the experimental and computational results above.

CONCLUSIONS

The synthesis and characterization of the direct ring-fluorinated and indirect trifluoromethyl-fluorinated nonfullerene acceptors **BTF** and **BTFM** are reported. We show that both direct and indirect fluorination modalities can significantly enhance the corresponding OSC performance under different fabrication conditions. Diverse suites of characterizations were applied to elucidate the differences between direct and indirect fluorination effects on the NFAs and their performance in bulk-heterojunction blends with the donor polymer **D18-Cl**. It can be seen that two fluorination modalities both red-shift the optical absorption profiles and lower the FMO energies. While **BTF** and **BTFM** have very similar solution absorption, **BTF** is more effective in red-shifting the absorption in the film state and lowering the FMO energies. Compared with indirectly fluorinated **BTFM**, directly fluorinated **BTF** shows greater crystallinity as indicated by the higher Tc and Tm. Single-crystal x-ray analysis indicates that **BTF** isomers form cocrystals in the single crystal unit cell with a close π- π stacking distance. In contrast, only the single-crystal of isomer **BTFM-1** is found in bulk **BTFM**, which indicates that it may possess a higher crystallinity or a lower solubility than the other two isomers. Also only **BTFM-1** has a close intermolecular CF_3-cyano group interaction and a unique EG-alkylchain bifurcated hydrogen-bond.[65, 67, 68] Different stacking motifs were examined in **BTF** and **BTFM-1**, and only the EG-EG stacking can propagate through the entire crystal network, whereas other stacking motifs are localized and gapped spatially. Photovoltaic measurements reveal an additive-dependent performance relationship, with 1-CN enhancing the performance of **D18-Cl**:**BTF**-based devices, while compromising that in **D18-Cl**:**BTFM**-based OSCs. SCLC measurements suggest that the 1-CN influences OSC performance by modifying the electron mobility, while hole mobility remains largely unchanged. DFT-level computation reveals multiple large electronic coupling neighbors and the low IREs in the **BTF** and **BTFM** crystal network which should enable efficient intermolecular exciton separation and transport. Also, as the F substitution position systematic varies from pointing outside to pointing inside, a decreasing trend in IREs was found in **BTF** and **BTFM**, which provides a design principle for future development of NFAs with low IREs.

Morphological characterization data indicate that the opposite response of device performance to the additive is most likely reflects microstructural differences in the BHJ layer acceptor domains, where HR-TEM, 2D GIWAXS, and RSoXS measurements confirm that the 1-CN additive reduces the overall **D18-Cl**:**BTF** blend film crystallinity, while promoting the overall **D18-Cl**:**BTFM-1** blend film crystallinity. These results suggest that a 'intermediate' level of BHJ layer crystallinity is essential to the performance of BHJ-type OSC devices. The fsTA spectra observed within the instrument response time indicate ultrafast hole transfer from the acceptor to the donor, and the nsTA data demonstrate that the films with 1-CN added have longer exciton lifetimes, consistent with the impedance-based analysis. This work first develops the synthesis of two new hexafluorinated NFAs with different EG fluorination modalities, which when blended with donor polymer **D18-Cl** afford PCEs as high as 17.3%. These metrics closely rival the current literature record of 18% and argue that OPVs remain a viable strategy for efficient solar energy capture. We believe that this contribution provides the community with a valuable EG strategy for developing efficient OSC NFAs, but also provides a comprehensive approach to understanding the fundamental interplay between NFA structure and exciton dynamics in BHJ OSCs.

Author Contributions

G. L. and L. F. contributed equally to this work. G. L., L. F., A. F. and T. J. M. conceived the idea. G. L. synthesized BTF and BTFM, characterized the physical properties (UV, CV, DSC, TGA, TEM, AFM), and grow the single crystals. L.F. fabricated and measured the solar cell devices and conducted SCLC measurements. S.M. and D.M.D conducted the GIWAXS measurement and the data analysis. L.O.J., K.L.K and G.C.S. performed the DFT computation. R.M.J., R.M.Y., M.R.W. conducted the fs/ns TA measurement and the data analysis. W. H. conducted the UPS measurement; R.M.P. conducted the GPC characterization; V.K.S. and M.C.H. conducted the IPDA measurement and the data analysis. G. L. and W. Z. performed the TEM analysis. G.L. and N.L. performed single-crystal structure analysis. All authors analysed the results and prepared the paper.

Conflicts of interest

Authors declare no conflicts of interest.

Acknowledgements

This work was supported by U.S. Office of Naval Research Contract #N00014-20-1-2116 (G.L.: material synthesis and characterizations; L.W.F.: photovoltaic device fabrication and measurement) and by the U.S. Department of Commerce, National Institute of Standards and Technology as part of the Center for Hierarchical Materials Design Award #-70NANB10H005 (S.M.:GIWAXS and RSoXS analysis), and the Northwestern University Materials Research Science and Engineering Center Award NSF DMR-1720139 (V.K.S.: impedance measurements). Theory development (KLK, LOJ, GCS) was supported by DOE grant DE-AC02-06CH11357. Transient optical spectroscopy was supported by the U. S. Department of Energy, Office of Science, Office of Basic Energy Sciences under Award DE-FG02-99ER14999 (MRW). This work made use of the EPIC, BioCryo, Keck-II, and/or SPID facilities of Northwestern's NUANCE Center, which received support from the Soft and Hybrid Nanotechnology Experimental (SHyNE) Resource (NSFECCS-1542205) and Northwestern University Materials Research Science and Engineering Center (NSF DMR-1720139). We thank the Integrated Molecular Structure Education and Research Center (IMSERC) for characterization facilities supported by Northwestern U.S. National Science Foundation (NSF) under NSF CHE1048773, Soft and Hybrid Nanotechnology Experimental (SHyNE) Resource (NSF NNCI-1542205), the State of Illinois, and International Institute for Nanotechnology (IIN). This work was supported by the Department of Energy under contract no. DE-AC02-05CH11231 and used resources at beamline 8-ID-E of the Advanced Photon Source, a U.S. Department of Energy (DOE) Office of Science User Facility operated for the DOE Office of Science by Argonne National Laboratory under Contract No. DE-AC02-06CH11357. This research used beamlines 7-ID-1 (SST-1) and 11-BM (CMS) of the National Synchrotron Light Source II, a U.S. Department of Energy (DOE) Office of Science User Facility operated for the DOE Office of Science by Brookhaven National Laboratory under Contract No. DE-SC0012704.This work (IPDA) made use of the MatCI Facility which receives support from the MRSEC Program (NSF DMR-1720139) of the Materials Research Center at Northwestern University. W. Zhu thanks the Open Foundation of State Key Laboratory of Electronic Thin Films and Integrated Devices (KFJJ202001, Unconventional Organic Nonlinear Optical Hybrid Materials and Devices) for partial financial support. Dr. Jianhua Chen, and Mr. Brendan Kerwin are acknowledged for their support on some characterization techniques. The theory research was also supported in part through the computational resources and staff contributions provided for the Quest high performance computing facility at Northwestern University which is jointly supported by the Office of the Provost, the Office for Research, and Northwestern University Information Technology. This work made use of the GIANTFab core facility at Northwestern University. GIANTFab is supported by the Institute for Sustainability and Energy at Northwestern and the Office of the Vice President for Research at Northwestern. Dr. Ding Zheng at Department of Chemistry, Northwestern University was acknowledged for his support in some characterizations. Note that certain commercial equipment, instruments, or materials are identified in this paper to specify the experimental procedure adequately. Such identification is not intended to imply recommendation or endorsement by NIST, nor is it intended to imply that the materials or equipment identified are necessarily the best available for the purpose.

Notes and references

1. K. A. Mazzio and C. K. Luscombe, *Chem. Soc. Rev.*, 2015, **44**, 78-90.
2. L. Y. Lu, T. Y. Zheng, Q. H. Wu, A. M. Schneider, D. L. Zhao and L. P. Yu, *Chem. Rev.*, 2015, **115**, 12666-12731.
3. P. Cheng, G. Li, X. Zhan and Y. J. N. P. Yang, *Nat. Photonics*, 2018, **12**, 131-142.
4. C. Yan, S. Barlow, Z. Wang, H. Yan, A. K.-Y. Jen, S. R. Marder and X. Zhan, *Nat. Rev. Mater.*, 2018, **3**, 1-19.
5. C. Lee, S. Lee, G.-U. Kim, W. Lee and B. J. Kim, *Chem. Rev.*, 2019, **119**, 8028-8086.
6. G. Wang, F. S. Melkonyan, A. Facchetti and T. J. Marks, *Angew. Chem. Int. Ed.*, 2019, **58**, 4129-4142.
7. B. Kan, Y. Kan, L. Zuo, X. Shi and K. Gao, *InfoMat*, 2021, **3**, 175-200.

8. Q. Liu, Y. Jiang, K. Jin, J. Qin, J. Xu, W. Li, J. Xiong, J. Liu, Z. Xiao, K. Sun, Y. Shangfeng, Z. Xiaotao and D. Liming, *Science Bulletin*, 2020, **65**, 272-275.
9. J. Wu, G. Li, J. Fang, X. Guo, L. Zhu, B. Guo, Y. Wang, G. Zhang, L. Arunagiri and F. J. N. c. Liu, *Nat. Commun.*, 2020, **11**, 1-9.
10. H. Sun, F. Chen and Z. K. Chen, *Mater. Today*, 2019, **24**, 94-118.
11. Q. Burlingame, M. Ball and Y.-L. Loo, *Nat. Energy*, 2020, **5**, 947-949.
12. Q. Yue, W. Liu and X. Zhu, *J. Am. Chem. Soc.*, 2020, **142**, 11613-11628.
13. J. Q. Zhang, H. S. Tan, X. G. Guo, A. Facchetti and H. Yan, *Nat. Energy*, 2018, **3**, 720-731.
14. G. Y. Zhang, J. B. Zhao, P. C. Y. Chow, K. Jiang, J. Q. Zhang, Z. L. Zhu, J. Zhang, F. Huang and H. Yan, *Chem. Rev.*, 2018, **118**, 3447-3507.
15. F. Lin, K. Jiang, W. Kaminsky, Z. Zhu and A. K. Y. Jen, *J. Am. Chem. Soc.*, 2020, **142**, 15246-15251.
16. P. Cheng, G. Li, X. W. Zhan and Y. Yang, *Nat. Photonics*, 2018, **12**, 131-142.
17. Y. Z. Lin, J. Y. Wang, Z. G. Zhang, H. T. Bai, Y. F. Li, D. B. Zhu and X. W. Zhan, *Adv. Mater.*, 2015, **27**, 1170-1174.
18. T. J. Aldrich, M. Matta, W. G. Zhu, S. M. Swick, C. L. Stern, G. C. Schatz, A. Facchetti, F. S. Melkonyan and T. J. Marks, *J. Am. Chem. Soc.*, 2019, **141**, 3274-3287.
19. W. Zhao, S. Li, H. Yao, S. Zhang, Y. Zhang, B. Yang and J. Hou, *J. Am. Chem. Soc.*, 2017, **139**, 7148-7151.
20. J. Yuan, Y. Zhang, L. Zhou, C. Zhang, T. K. Lau, G. Zhang, X. Lu, H. L. Yip, S. K. So, S. Beaupré, M. Mainville, P. A. Johnson, M. Leclerc, H. Chen, H. Peng, Y. Li and Y. Zou, *Adv. Mater.*, 2019, **31**, 1807577.
21. G. Li, X. Zhang, L. O. Jones, J. M. Alzola, S. Mukherjee, L.-W. Feng, W. Zhu, C. L. Stern, W. Huang, J. Yu, V. K. Sangwan, D. M. DeLongchamp, K. L. Kohlstedt, M. R. Wasielewski, M. C. Hersam, G. C. Schatz, A. Facchetti and T. J. Marks, *J. Am. Chem. Soc.*, 2021, **143**, 6123-6139.
22. J. Yuan, Y. Q. Zhang, L. Y. Zhou, G. C. Zhang, H. L. Yip, T. K. Lau, X. H. Lu, C. Zhu, H. J. Peng, P. A. Johnson, M. Leclerc, Y. Cao, J. Ulanski, Y. F. Li and Y. P. Zou, *Joule*, 2019, **3**, 1140-1151.
23. J. Zhang, H. S. Tan, X. Guo, A. Facchetti and H. Yan, *Nat Energy*, 2018, **3**, 720-731.
24. G. Zhang, J. Zhao, P. C. Y. Chow, K. Jiang, J. Zhang, Z. Zhu, J. Zhang, F. Huang and H. Yan, *Chem Rev*, 2018, **118**, 3447-3507.
25. A. Wadsworth, M. Moser, A. Marks, M. S. Little, N. Gasparini, C. J. Brabec, D. Baran and I. McCulloch, *Chem Soc Rev*, 2019, **48**, 1596-1625.
26. Y. Chen, Y. Zheng, Y. Jiang, H. Fan and X. Zhu, *J. Am. Chem. Soc.*, 2021, **143**, 4281-4289.
27. Z. Zhou, W. Liu, G. Zhou, M. Zhang, D. Qian, J. Zhang, S. Chen, S. Xu, C. Yang, F. Gao, H. Zhu, F. Liu and X. Zhu, *Adv. Mater.*, 2020, **32**, 1906324.
28. C. Sun, F. Pan, S. Chen, R. Wang, R. Sun, Z. Shang, B. Qiu, J. Min, M. Lv, L. Meng, C. Zhang, M. Xiao, C. Yang and Y. Li, *Adv Mater*, 2019, **31**, 1905480.
29. T. Yan, W. Song, J. Huang, R. Peng, L. Huang and Z. Ge, *Adv Mater*, 2019, **31**, 1902210.
30. S. Li, C.-Z. Li, M. Shi and H. Chen, *ACS Energy Letters*, 2020, **5**, 1554-1567.
31. L. Liu, Y. Kan, K. Gao, J. Wang, M. Zhao, H. Chen, C. Zhao, T. Jiu, A.-K.-Y. Jen and Y. Li, *Adv Mater*, 2020, **32**, 1907604.
32. Q. Liu, Y. Jiang, K. Jin, J. Qin, J. Xu, W. Li, J. Xiong, J. Liu, Z. Xiao, K. Sun, S. Yang, X. Zhang and L. Ding, *Science Bulletin*, 2020, **65**, 272-275.
33. C. Li, J. Zhou, J. Song, J. Xu, H. Zhang, X. Zhang, J. Guo, L. Zhu, D. Wei, G. Han, J. Min, Y. Zhang, Z. Xie, Y. Yi, H. Yan, F. Gao, F. Liu and Y. Sun, *Nat. Energy*, 2021, **6**, 605-613.
34. H. Sun, T. Liu, J. Yu, T.-K. Lau, G. Zhang, Y. Zhang, M. Su, Y. Tang, R. Ma, B. Liu, L. Jiaen, F. Kui, L. Xinhui, G. Xugang, G. Feng and Y. He, *Energy Environ. Sci.*, 2019, **12**, 3328-3337.
35. F. Liu, Z. Zhou, C. Zhang, T. Vergote, H. Fan, F. Liu and X. Zhu, *J. Am. Chem. Soc.*, 2016, **138**, 15523-15526.
36. Z. R. Grabowski, K. Rotkiewicz and W. Rettig, *Chem. Rev.*, 2003, **103**, 3899-4031.
37. W. Xue, Y. Tang, X. Zhou, Z. Tang, H. Zhao, T. Li, L. Zhang, S. Liu, C. Zhao, W. Ma and H. Yan, *Adv. Funct. Mater.*, 2021, **31**, 2101892.
38. W. Gao, M. Zhang, T. Liu, R. J. Ming, Q. S. An, K. L. Wu, D. J. Xie, Z. H. Luo, C. Zhong, F. Liu, F. J. Zhang, H. Yan and C. L. Yang, *Adv. Mater.*, 2018, **30**.
39. J. F. Qu, D. N. Li, H. Wang, J. D. Zhou, N. Zheng, H. J. Lai, T. Liu, Z. Q. Xie and F. He', *Chem. Mater.*, 2019, **31**, 8044-8051.
40. S. M. Swick, W. G. Zhu, M. Matta, T. J. Aldrich, A. Harbuzaru, J. T. L. Navarrete, R. P. Ortiz, K. L. Kohlstedt, G. C. Schatz, A. Facchetti, F. S. Melkonyan and T. J. Marks, *Proc. Natl. Acad. Sci. U. S. A.*, 2018, **115**, E8341-E8348.
41. S. X. Dai, J. D. Zhou, S. Chandrabose, Y. J. Shi, G. C. Han, K. Chen, J. M. Xin, K. Liu, Z. Y. Chen, Z. Q. Xie, W. Ma, Y. P. Yi, L. Jiang, J. M. Hodgkiss and X. W. Zhan, *Adv. Mater.*, 2020, **32**.
42. S. Y. Feng, M. Li, N. N. Tang, X. D. Wang, H. Huang, G. L. Ran, Y. H. Liu, Z. Q. Xie, W. K. Zhang and Z. S. Bo, *ACS Appl. Mater. Interfaces*, 2020, **12**, 4638-4648.
43. S. M. Swick, J. M. Alzola, V. K. Sangwan, S. H. Amsterdam, W. Zhu, L. O. Jones, N. Powers-Riggs, A. Facchetti, K. L. Kohlstedt, G. C. Schatz, M. C. Hersam, M. R. Wasielewski and T. J. Marks, *Adv. Energy Mater.*, 2020, **10**, 2000635.
44. S. X. Dai, F. W. Zhao, Q. Q. Zhang, T. K. Lau, T. F. Li, K. Liu, Q. D. Ling, C. R. Wang, X. H. Lu, W. You and X. W. Zhan, *J. Am. Chem. Soc.*, 2017, **139**, 1336-1343.
45. J. Chen, Y. Chen, L.-W. Feng, C. Gu, G. Li, N. Su, G. Wang, S. M. Swick, W. Huang, X. Guo, A. Facchetti and T. J. Marks, *EnergyChem*, 2020, **2**, 100042.
46. W. G. Zhu, A. P. Spencer, S. Mukherjee, J. M. Alzola, V. K. Sangwan, S. H. Amsterdam, S. M. Swick, L. O. Jones, M. C. Heiber, A. A. Herzing, G. P. Li, C. L. Stern, D. M. DeLongchamp, K. L. Kohlstedt, M. C. Hersam, G. C. Schatz, M. R. Wasielewski, L. X. Chen, A. Facchetti and T. J. Marks, *J. Am. Chem. Soc.*, 2020, **142**, 14532-14547.
47. X. Ma, A. Zeng, J. Gao, Z. Hu, C. Xu, J. H. Son, S. Y. Jeong, C. Zhang, M. Li, K. Wang, H. Yan, Z. Ma, Y. Wang, H. Y. Woo and F. Zhang, *Natl. Sci. Rev.*, 2020, **8**.
48. M. Li, A. H. Balawi, P. J. Leenaers, L. Ning, G. H. Heintges, T. Marszalek, W. Pisula, M. M. Wienk, S. C. Meskers, Y. Yi, F. Laquai and R. A. J. Janssen, *Nat. Commun.*, 2019, **10**, 1-11.
49. L. W. Feng, J. H. Chen, S. Mukherjee, V. K. Sangwan, W. Huang, Y. Chen, D. Zheng, J. W. Strzalka, G. Wang, M. C. Hersam, D. M. DeLongchamp, A. Facchetti and T. J. Marks, *ACS Energy Lett.*, 2020, **5**, 1780-1787.
50. S. M. Swick, W. Zhu, M. Matta, T. J. Aldrich, A. Harbuzaru, J. T. Lopez Navarrete, R. Ponce Ortiz, K. L. Kohlstedt, G. C. Schatz, A. Facchetti, F. S. Melkonyan and T. J. Marks, *Proc. Natl. Acad. Sci. U. S. A.*, 2018, **115**, E8341.
51. L. Yu, D. Qian, S. Marina, F. A. A. Nugroho, A. Sharma, S. Hultmark, A. I. Hofmann, R. Kroon, J. Benduhn, S. Detlef, K. Vandewal, M. R. Andersson, C. Langhammer, J. Martín, F. Gao and C. Müller, *ACS Appl. Mater. Interfaces*, 2019, **11**, 21766-21774.
52. J. Nelson, *Phys. Rev. B*, 2003, **67**, 155209.
53. J. Yuan, T. Huang, P. Cheng, Y. Zou, H. Zhang, J. L. Yang, S.-Y. Chang, Z. Zhang, W. Huang, R. Wang, D. Meng, F. Gao and Y. Yang, *Nat. Commun.*, 2019, **10**, 570.
54. D. Qian, Z. Zheng, H. Yao, W. Tress, T. R. Hopper, S. Chen, S. Li, J. Liu, S. Chen, J. Zhang, X.-K. Liu, B. Gao, L. Ouyang, Y. Jin, G. Pozina, I. A. Buyanova, W. M. Chen, O. Inganäs, V. Coropceanu, J.-L. Bredas, H. Yan, J. Hou, F. Zhang, A. A. Bakulin and F. Gao, *Nat. Mater.*, 2018, **17**, 703-709.
55. C. McDowell, M. Abdelsamie, M. F. Toney and G. C. Bazan, *Adv. Mater.*, 2018, **30**, 1707114.
56. A. K. K. Kyaw, D. H. Wang, C. Luo, Y. Cao, T.-Q. Nguyen, G. C. Bazan and A. J. Heeger, *Adv. Energy Mater.*, 2014, **4**, 1301469.
57. E. F. Manley, J. Strzalka, T. J. Fauvell, T. J. Marks and L. X. Chen, *Adv. Energy Mater.*, 2018, **8**, 1800611.
58. J. Lv, H. Tang, J. Huang, C. Yan, K. Liu, Q. Yang, D. Hu, R. Singh, J. Lee, S. Lu, G. Li and Z. Kan, *Energy Environ. Sci.*, 2021, **14**, 3044-3052.
59. Y. Zhang, A. J. Parnell, F. Pontecchiani, J. F. K. Cooper, R. L. Thompson, R. A. L. Jones, S. M. King, D. G. Lidzey and G. Bernardo, *Scientific Reports*, 2017, **7**, 44269.
60. S. J. Lou, N. Zhou, X. Guo, R. P. H. Chang, T. J. Marks and L. X. Chen, *J. Mater. Chem. A*, 2018, **6**, 23805-23818.
61. J. Kniepert, I. Lange, J. Heidbrink, J. Kurpiers, T. J. K. Brenner, L. J. A. Koster and D. Neher, *J. Phys. Chem. C*, 2015, **119**, 8310-8320.
62. H. Huang, L. Yang, A. Facchetti and T. J. Marks, *Chem. Rev.*, 2017, **117**, 10291-10318.
63. J. Chen, Q. Liao, G. Wang, Z. Yan, H. Wang, Y. Wang, X. Zhang, Y. Tang, A. Facchetti, T. J. Marks and X. Guo, *Macromolecules*, 2018, **51**, 3874-3885.
64. M. T. Scerba, S. Bloom, N. Haselton, M. Siegler, J. Jaffe and T. Lectka, *J. Org. Chem.*, 2012, **77**, 1605-1609.
65. N. Lu, V. Elakkat, J. S. Thrasher, X. Wang, E. Tessema, K. L. Chan, R.-J. Wei, T. Trabelsi and J. S. Francisco, *J. Am. Chem. Soc.*, 2021, **143**, 5550-5557.
66. E. S. Feldblum and I. T. Arkin, *Proc. Natl. Acad. Sci. U. S. A.*, 2014, **111**, 4085.
67. V. Elakkat, C.-C. Chang, J.-Y. Chen, Y.-C. Fang, C.-R. Shen, L.-K. Liu and N. Lu, *Chem. Commun.*, 2019, **55**, 14259-14262.
68. N. Lu, W.-H. Tu, Y.-S. Wen, L.-K. Liu, C.-Y. Chou and J.-C. Jiang, *CrystEngComm*, 2010, **12**, 538-542.
69. L. Jones and L. Lin, *Comput. Theor. Chem.*, 2017, **1115**, 22-29.
70. S. M. Swick, T. Gebraad, L. Jones, B. Fu, T. J. Aldrich, K. L. Kohlstedt, G. C. Schatz, A. Facchetti and T. J. Marks, *Chemphyschem*, 2019, **20**, 2608-2626.
71. Q. D. Truong, M. K. Devaraju, T. Tomai and I. Honma, *ACS Appl. Mater. Interfaces*, 2013, **5**, 9926-9932.
72. O. L. Krivanek, M. F. Chisholm, V. Nicolosi, T. J. Pennycook, G. J. Corbin, N. Dellby, M. F. Murfitt, C. S. Own, Z. S. Szilagyi, M. P. Oxley, S. T. Pantelides and S. J. Pennycook, *Nature*, 2010, **464**, 571-574.
73. Y. C. Lin, Y. J. Lu, C. S. Tsao, A. Saeki, J. X. Li, C. H. Chen, H. C. Wang, H. C. Chen, D. Meng, K. H. Wu, Y. Yang and K. H. Wei, *J. Mater. Chem. A*, 2019, **7**, 3072-3082.
74. C.-Y. Liao, Y. Chen, C.-C. Lee, G. Wang, N.-W. Teng, C.-H. Lee, W.-L. Li, Y.-K. Chen, C.-H. Li and H.-L. Ho, *Joule*, 2020, **4**, 189-206.
75. D.-M. Smilgies, *J. Appl. Crystallogr.*, 2009, **42**, 1030-1034.
76. G. Wang, L.-W. Feng, W. Huang, S. Mukherjee, Y. Chen, D. Shen, B. Wang, J. Strzalka, D. Zheng, F. Melkonyan, J. Yan, F. J. Stoddart, D. M. DeLongchamp, M. Zhu, A. Facchetti and T. J. Marks, *Proc. Natl. Acad. Sci. U. S. A.*, 2020, **117**, 17551-17557.

77. M. C. Heiber, T. Okubo, S. J. Ko, B. R. Luginbuhl, N. A. Ran, M. Wang, H. B. Wang, M. A. Uddin, H. Y. Woo, G. C. Bazan and T. Q. Nguyen, *Energy Environ. Sci.*, 2018, **11**, 3019-3032.
78. N. Su, R. Ma, G. Li, T. Liu, L.-W. Feng, C. Lin, J. Chen, J. Song, Y. Xiao, J. Qu, X. Lu, V. K. Sangwan, M. C. Hersam, H. Yan, A. Facchetti and T. J. Marks, *ACS Energy Lett.*, 2021, **6**, 728-738.
79. D. Bartesaghi, I. D. Perez, J. Kniepert, S. Roland, M. Turbiez, D. Neher and L. J. A. Koster, *Nat. Commun.*, 2015, **6**, 7083.